The Vibrational State Dependence of the ^{14}N Quadrupole Coupling Tensor in Aniline. A Microwave Fourier-Transform Study Combined with Semirigid Bender Calculations

B. Kleibömer and D. H. Sutter
Abteilung Chemische Physik im Institut für Physikalische Chemie der Universität Kiel

Z. Naturforsch. **43a**, 561–571 (1988); received March 22, 1988

Experimental values for the diagonal elements of the ^{14}N quadrupole coupling tensor derived from analysis of the hyperfine structure of low-J rotational transitions are reported for the two lowest states of the amino wagging mode. They show the expected difference due to averaging over the large amplitude amino wag.

A semirigid bender analysis of previously published infrared data provides the inversion angle expectation values for use in a quantum-chemical calculation of the corresponding effective Coulomb field gradients at the nitrogen nucleus.

The results are compared to those obtained earlier for the related molecules vinylamine, cyanamide and ammonia.

Introduction

From earlier microwave spectroscopic studies [1, 2, 3] aniline is known to have an essentially planar heavy atom skeleton with a pyramidal NH_2 group attached to it. Its ^{14}N nuclear quadrupole coupling constants, its electric dipole moment and a complete substitution structure have been determined in these studies.

The rotational spectrum of aniline consists of doublets due to molecules in the two lowest states of the inversion motion of the amino group. This large amplitude motion renders the determination of the structural parameters of the NH_2-group by the substitution method [4] unprecise, and therefore recently a partial equilibrium structure has been determined by explicitely treating the anharmonicity of the inversion motion and including the effective rotational constants in two or more inversion states [5].

In the study reported here, we have investigated the ^{14}N quadrupole hyperfine splittings of the rotational transitions of molecules in the two lowest states of the inversion motion. With the superior resolution and sensitivity of our new microwave Fourier-transform spectrometer, the differences of the splittings in the 0^+-state and in the 0^--state could be measured for the first time.

Reprint requests to Prof. Dr. D. H. Sutter, Abteilung Chemische Physik im Institut für Physikalische Chemie der Christian-Albrechts-Universität Kiel, D-2300 Kiel, Olshausenstr. 40 FRG.

In the first part of the paper we give some informations on the microwave Fourier-transform spectrometer.

In the second part we present our analysis of the splittings and our interpretation of the results within a semirigid bender model. This includes a comparison with the quadrupole coupling constants obtained earlier for the related molecules vinylamine, cyanamide and ammonia.

The Microwave Fourier-transform Spectrometer

A simplified block diagram of our spectrometer is shown in Figure 1. In a typical experiment the cw polarization microwave source (upper center), locked to the n-th harmonic of a frequency synthesizer (left), is first set close to the rotational resonances under investigation (off-resonance setting is usually less than 1 MHz). The microwave radiation is chopped into short pulses by PIN-diode-switch 1. The pulse duration is adjustable between 10 ns and up to 25 µs, with 100 ns a typical value in routine work. The pulses are then amplified into the 1 to 20 W range by a travelling wave tube amplifier (TWTA). In the sample cell those subensembles of molecules which can undergo an electric dipole transition to an eigenstate with a transition frequency sufficiently close to the microwave frequency in the incident pulse, are coherently driven into a mixed state. The degree of this mixing depends on the dipole matrix element, on the field strength of

0932-0784 / 88 / 0600-0561 $ 01.30/0. – Please order a reprint rather than making your own copy.

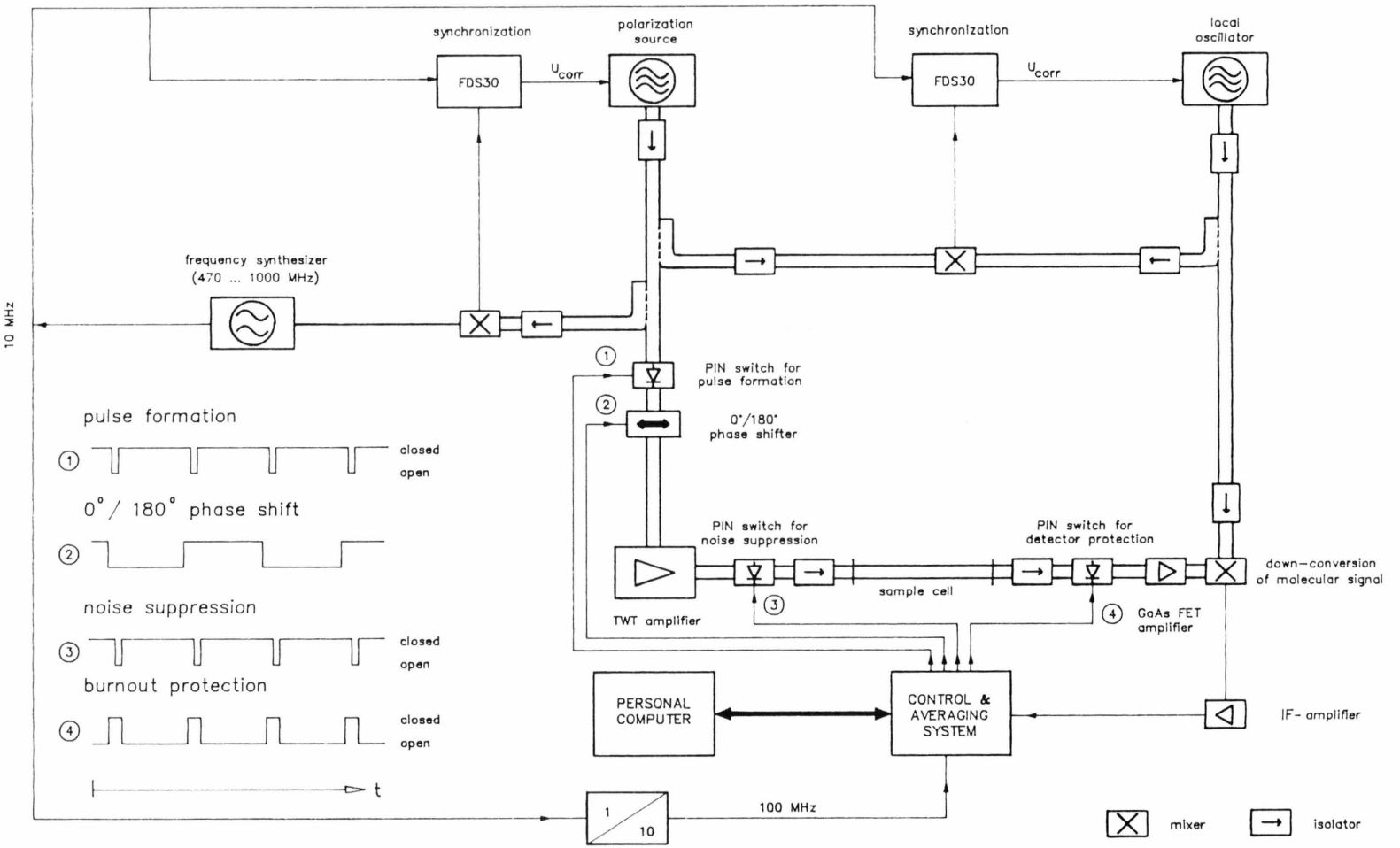

Fig. 1. Block diagram of the microwave Fourier-transform spectrometer used in the present investigation. The sample (sample pressure below 10^{-3} mbar) is polarized by short, near-resonant microwave pulses. The resulting coherent emission signal is then amplified and heterodyned down into the 30 MHz range. After digitization and averaging, the observed transient emission signals are subjected to a discrete Fourier-transformation or to a non-linear least-squares fit procedure to yield the molecular transition frequencies, intensities and linewidths. For more details see text.

the driving microwave field, on the off-resonance and on the pulse duration [6–9]. After the pulse the subensembles in turn emit their corresponding molecular transition frequencies. This molecular emission decays within few microseconds, since collisions and Doppler dephasing destruct the coherence. The faint molecular emission signal, typically 10^{-13} to 10^{-11} W, is amplified by a low-noise GaAs-FET amplifier and is then heterodyned down into the 30 MHz range in a double-balanced mixer (lower right). (The local oscillator (upper right) is phase-locked to the polarization oscillator at a frequency exactly 30 MHz above (or below) the frequency of the latter). The i.f. signal corresponding to the molecular emission signal is amplified and digitized at a rate of typically 100 MHz, i.e. every 10 ns a sample is taken. With signal to noise ratios on the order of 1/100 to 1/10 at the input of the digitizer, typically 10^6 decays are averaged up before further processing the data. To guarantee correct phase relations between subsequent decays [10], pulsing and data acquisition are locked to the same master clock as is used in phase-locking the local oscillator to the polarization oscillator. The block diagram also shows some additional details:

1) For pulse echo suppression, waveguide ferrite isolators, which attenuate microwaves travelling in the reverse direction by more than 20 dB, are inserted at either end of the sample cell.
2) Additional PIN-diode-switches protect the sensitive GaAs-FET amplifier against burnout during the pulses (switch 4) and block TWTA noise during the transient emission periods (switch 3).
3) A 180° phase alternation between subsequent pulses is used to discriminate between signals of molecular origin (they shift phase) and coherent pickups within the electronics (they do not shift phase).

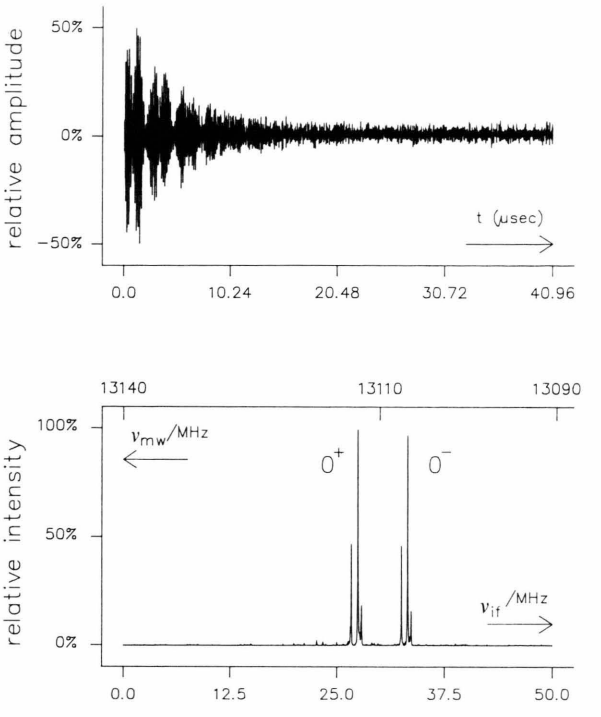

Fig. 2. Transient molecular emission signal (above) and the corresponding Fourier-transform power spectrum (below) of the inversion doublet of the $3_{22} - 2_{21}$ rotational transition of aniline-NH_2. The molecules were polarized by a pulse of 80 ns duration with a carrier frequency at 13 109.988 MHz, near the center of the 0^+- and 0^--components. For each decay 4 k data points were recorded in 10 ns intervals. 0.984 million decays were averaged up. The triplet splitting of the 0^+- and 0^--components is due to the ^{14}N-quadrupole coupling. Spin weights, 9 for the upper 0^--state and 7 for the lower 0^+-state, and the vibrational Boltzmann factors almost compensate at the sample temperature of −30 °C, giving rise to a doublet of almost identical intensities. The sample pressure was 2 mTorr.

The timing for the PIN-swith pulses and for the phase shift sequence is shown as an insert at left in Figure 1. In Fig. 2 we show a typical transient decay and its Fourier-transform power spectrum.

The heart of the spectrometer is a new averager (Fig. 1, bottom right). At its input the transient molecular emission signal, which is deeply buried in instrumental noise, is probed every 10 ns by a fast comparator. Depending on the sign of the input voltage a plus-one or a minus-one is added to the contents of the appropriate memory cell in the 4 k 16-bit RAM. For the convenience of the reader, the mathematical background of 1-bit averaging is described in the Appendix with special emphasis on our application. Parallel processing in 16 data paths makes it possible to perform AD-conversion (fast) and data accumulation (slow) simultaneously and thus to run the experiment at a repetition rate, which is about three times larger than with the previous design [11]. Furthermore, with the RAM increased from 1 k to 4 k, also slower decays can now be probed over a period of up to 40 μs with the short sampling interval of only 10 ns. Both improvements, higher repetition rate and increased RAM space, have led to a significant improvement in the signal to noise ratio which can be obtained in a given amount of time. The latter improvement also has minimized problems with "aliasing" which was common with the previous design, if slow decays were studied. The new averager is described in detail in a separate publication [12].

Experimental Details and Analysis of the Rotational Hyperfine Splittings

The quadrupole hyperfine splittings of four R-branch and three Q-branch rotational transitions of aniline in the 0^+- and 0^--state of the NH_2 inversion motion were measured with the spectrometer described in the previous section. Sample temperatures were close to $-30\,^\circ C$ and sample pressures were close to 1 mTorr (0.13 Pa). We also observed a number of vibrational satellites, some of them appearing as doublets. Most likely they are the 0^+- and 0^--components of the first excited state of a vibration other than the inversion. Four lines, not closely accompanied by other lines, could be fitted by an effective rigid rotor Hamiltonian and were tentatively assigned as originating from molecules in the 1^+-state of the NH_2 inversion, since in the 1^+- and 1^--states the "inversion splitting" is so large that the corresponding rotational transition, which originates from molecules in the upper 1^--state, should appear as an isolated line well separated from its observed 1^+-partner and far weaker in intensity due to the Boltzmann factor (compare Figure 3).

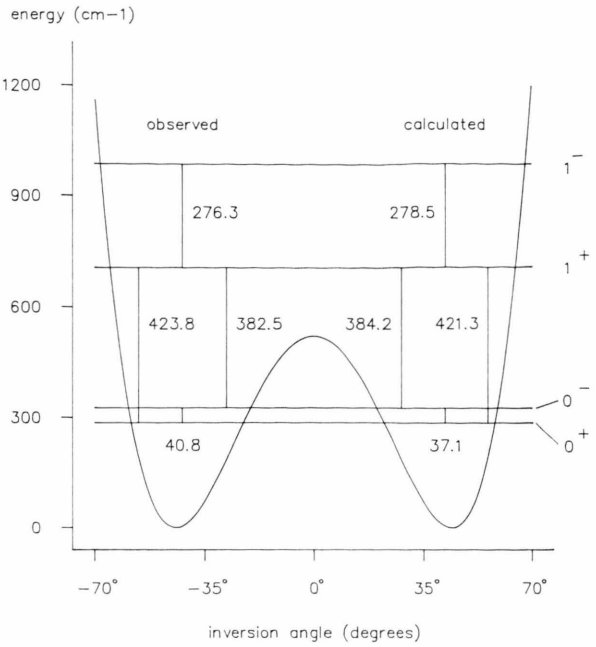

Fig. 3. Potential for the NH_2 inversion of aniline with observed [27] and calculated inversion band wavenumbers. The latter were calculated within the semirigid bender model described in the text using the optimized potential function $V(\tau)/cm^{-1} = 1511\,\tau^4/rad^4 - 1806\,\tau^2/rad^2 + 540$. For the definition of the inversion angle τ compare Figure 6.

In Table 1 we present a list of measured frequencies. The transition frequencies were determined by a least-squares fit of the frequencies, amplitudes, phases and relaxation times to the observed decays [13]. This procedure yields considerably more accurate results than the traditional discrete Fourier-transform analysis of the decays [14, 15]. The least-squares standard deviations are typically on the order of 1 kHz or below for the stronger satellites and up to 2 kHz for the weaker satellites listed in Table 1. This agrees with the reproducibility of the frequencies when the experiments were repeated at an other day and with slightly different microwave frequencies in the exciting pulses. It also agrees with the quality of the fit of the ^{14}N quadrupole hyperfine structure within first order quadrupole coupling theory [16]. In the corresponding Hamiltonian, the rotational constants and ^{14}N quadrupole coupling constants are effective values. In principle they originate from a second order perturbation treatment within the vibronic states i.e. a Van Vleck transformation [17], which aims at the state under consideration. In our case they are essentially the vibronic expectation values of the corresponding operators. The averaging over the inversion motion is discussed below. The only term which leads to matrix elements between the closely spaced 0^+- and 0^--levels arises from the inertia tensor element μ_{xz} (see (2) below). However, it is so small that a second order Van Vleck treatment is adequate. (μ_{xz} does not contribute to first order since its expectation value vanishes due to symmetry.)

The center frequencies of the hfs-multiplets were then used for a fit of the effective rotational constants. Our results are presented in Table 2. Also given for comparison are the corresponding values determined earlier by Lister et al. [3] who, however, did not give their experimental uncertainties. In Table 3 we present our ^{14}N quadrupole hfs coupling constants together with the effective inversion angle $\tau_{eff}, v = \sqrt{\langle \psi_v | \tau^2 | \psi_v \rangle}$ and expectation values for some even powers of τ. Compared to the previous work by Hatta et al. [2], who could not measure the difference of the hfs-splittings in the 0^+- and 0^--states, the standard deviations of the coupling constants are reduced by more than an order of magnitude. Also given in Table 3 are the corresponding values for the related molecules cyanamide, vinylamine and ammo-

Table 1. ^{14}N quadrupole hyperfine splittings of some low-J rotational transitions of aniline in the 0^+- and 0^--state of the NH_2 inversion. Also given are some splittings tentatively assigned to molecules in the 1^+-state. The experimental frequencies were obtained from a decay-fit procedure described earlier [13]. The theoretical splittings were calculated within the rigid rotor model using the optimized quadrupole coupling constants presented in Table 3. Frequencies are given in MHz.

		Observed frequency	Splitting/MHz		Observed frequency	Splitting/MHz		Observed frequency	Splitting/MHz	
			$\Delta\nu_{exp}$	$\Delta\nu_{calc}$		$\Delta\nu_{exp}$	$\Delta\nu_{calc}$		$\Delta\nu_{exp}$	$\Delta\nu_{calc}$
$3_{03}-2_{02}$	4 – 3	12 562.923	−0.109	−0.109	12 558.668	−0.105	−0.104	12 570.214	−0.110	−0.108
	2 – 1	12 563.008	−0.024	−0.022	12 558.752	−0.021	−0.021			
	3 – 2	12 563.251	0.219	0.218	12 558.982	0.209	0.209	12 570.542	+0.218	+0.217
$3_{22}-2_{21}$	2 – 1	13 112.089	−0.597	−0.596	13 106.328	−0.570	−0.570	13 122.034	−0.586	−0.588
	4 – 3	13 112.516	−0.170	−0.170	13 106.735	−0.163	−0.163	13 122.448	−0.172	−0.168
	3 – 2	13 113.282	0.596	0.596	13 107.469	0.571	0.570	13 123.209	+0.589	+0.588
$3_{21}-2_{20}$	2 – 1	13 661.895	−0.453	−0.455	13 654.596	−0.432	−0.434	13 674.459	−0.445	−0.447
	4 – 3	13 662.257	−0.092	−0.090	13 654.939	−0.089	−0.086	13 674.813	−0.091	−0.088
	3 – 2	13 662.727	0.379	0.378	13 665.390	0.362	0.361	13 675.276	+0.372	+0.371
$3_{12}-2_{11}$	2 – 1	14 238.021	−0.254	−0.259	14 230.568	−0.244	−0.248			
	4 – 3	14 238.227	−0.049	−0.048	14 230.764	−0.048	−0.045	14 246.717	−0.043	−0.047
	3 – 2	14 238.480	0.205	0.209	14 231.010	0.198	0.200	14 246.062	0.202	0.207
$8_{26}-8_{27}$	8 – 8	14 930.443	−0.939	−0.941	14 901.313	−0.904	−0.901			
	9 – 9	14 931.778	0.396	0.396	14 902.596	0.379	0.379			
	7 – 7	14 931.945	0.563	0.564	14 902.761	0.544	0.541			
$6_{15}-6_{16}$	6 – 6	15 945.503	−1.253	−1.251	15 922.557	−1.197	−1.198			
	7 – 7	15 947.256	0.501	0.500	15 924.232	0.478	0.479			
	5 – 5	15 947.553	0.797	0.796	15 924.516	0.762	0.763			
$5_{24}-5_{05}$	5 – 5	17 311.386	−0.916	−0.916	17 298.632	−0.877	−0.877			
	6 – 6	17 312.655	0.352	0.352	17 299.848	0.339	0.337			
	4 – 4	17 312.913	0.611	0.611	17 300.091	0.582	0.585			

Table 2. Rigid rotor fit of effective rotational constants for aniline to the observed center frequencies of the ^{14}N quadrupole hyperfine multiplets given in Table 1. All values are given in MHz. For comparison the rotational constants determined by Lister and Tyler (Chem. Comm. **1966,** 152) are given in brackets.

$J'_{K'_-K'_+}-J_{K_-K_+}$	0^+-state		0^--state		1^+(?)-state	
	ν_{obs}	ν_{calc}	ν_{obs}	ν_{calc}	ν_{obs}	ν_{calc}
$3_{03}-2_{02}$	12 563.032	12 563.045	12 558.773	12 558.786	12 570.324	12 570.326
$3_{22}-2_{21}$	13 112.686	13 112.693	13 106.898	13 106.904	13 122.619	13 122.616
$3_{21}-2_{20}$	13 662.349	13 622.340	13 655.028	13 655.021	13 674.904	13 674.906
$3_{12}-2_{11}$	14 238.275	14 238.264	14 230.812	14 320.800	14 246.759	14.246.759
$5_{24}-5_{05}$	17 312.302	17 312.328	17 299.508	17 299.533		
$6_{15}-6_{16}$	15 946.756	15 946.689	15 923.754	15 923.689		
$8_{26}-8_{27}$	14 931.382	14 931.425	14 902.217	14 902.259		
A	5617.478 (12)	(5617.40)	5615.484 (12)	(5615.57)	5595.778 (22)	
B	2593.8591 (36)	(2593.83)	2592.2346 (36)	(2592.24)	2595.2377 (11)	
C	1777.0384 (36)	(1777.04)	1776.7332 (36)	(1776.73)	1778.9675 (11)	

nia. We observe that there is a significant inversion state dependence in the effective quadrupole coupling constants. The absolute values are larger in the 0^+-state and smaller in the 0^--state. The difference can even be seen in the power spectra such as the one shown in Figure 4.

The same trend in the dependence of the quadrupole coupling constants on the inversion state was observed earlier for the related molecules cyanamide and vinylamine [18].

This trend can be "understood" already within the simple minded picture of an sp^3 hybridized nitrogen in

Table 3. Effective ^{14}N quadrupole coupling constants observed for aniline-NH_2 in different states of the NH_2-inversion and expectation values for even powers of the inversion angle τ. (Odd power expectation values are zero from symmetry). Also given for comparison are the corresponding values for the related molecules cyanamide [18], vinylamine [18] and ammonia [30]. The τ^n-expectation values for ammonia were calculated within the rigid bender model using the NH bond distance and potential function given by D. Papousek, J. M. R. Stone, and V. Spirko [31].

Molecule	Inversion state	^{14}N-quadrupole coupling constants			Expectation values for τ^{2n} $(n=1,2,3)$		
		χ_{aa}/MHz	χ_{bb}/MHz	χ_{cc}/MHz	$\langle\tau^2\rangle$/rad^2	$\langle\tau^4\rangle$/rad^4	$\langle\tau^6\rangle$/rad^6
Aniline	0^+	2.3844 (41)	1.8424 (37)	−4.2268	0.4390	0.2928	0.2409
	0^-	2.2791 (45)	1.7667 (40)	−4.0458	0.5300	0.3729	0.3155
	1^+(?)	2.3506(108)	1.8312(401)	−4.1818	0.3552	0.3170	0.3296
	1^-	–	–	–	0.5429	0.5220	0.5904
Cyanamide	0^+	3.1241(107)	1.8207 (77)	−4.9448	0.4567	0.3163	0.2663
	0^-	3.0246 (78)	1.7201 (65)	−4.7447	0.5748	0.4272	0.3739
	1^+	3.1101(137)	1.5169(238)	−4.6270	0.4324	0.4124	0.4473
	1^-	3.0091(122)	1.6446(182)	−4.6537	0.6403	0.6625	0.7876
Vinylamine	0^+	2.0722 (76)	2.0751 (56)	−4.1473	0.4836	0.3722	0.3529
	0^-	1.9016(104)	2.0128 (90)	−3.9144	0.6466	0.5450	0.5438
Ammonia	0^+			−4.116 (2)	0.5812	0.3957	0.3035
	0^-			−4.112 (2)	0.5822	0.3970	0.3047
	1^+			−4.438(18)	0.4672	0.3789	0.3718
	1^-			−4.263(18)	0.5232	0.4315	0.4266
	2^+			–	0.3428	0.3214	0.3554
	2^-			–	0.5272	0.5162	0.5935

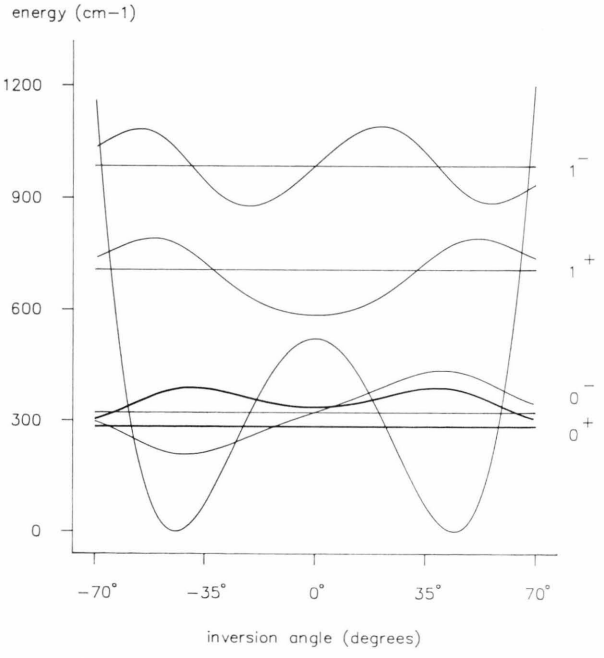

Fig. 4. Inversion potential and wavefunctions from the semi-rigid bender fit to the aniline-NH_2 far infrared data [27]. Due to the node in the planar configuration, the effective inversion angle, $\tau_{\text{eff},v} = \sqrt{\langle\psi_v|\tau^2|\psi_v\rangle}$, is larger in the 0^--state than in the 0^+-state.

the pyramidal configuration with an electron lone pair in the sp^3 orbital not involved in the σ-bonds to the ring and to the hydrogens, respectively, and a change in hybridization to sp^2 when the molecule swings through the planar configuration with the lone pair now in the nitrogen p-orbital perpendicular to the plane of the molecule. Just as described in a recent paper on the monofluorobenzonitriles [19], a simple Townes-Dailey type calculation of the quadrupole coupling constants leads to

$$\chi_{xx} = 2.5\,\text{MHz}, \quad \chi_{yy} = 3.75\,\text{MHz}, \quad \chi_{zz} = -6.25\,\text{MHz}$$

for the sp^3 case and to

$$\chi_{xx} = 5\,\text{MHz}, \quad \chi_{yy} = 5\,\text{MHz}, \quad \chi_{zz} = -10\,\text{MHz}$$

for the sp^2 case. (x-axis parallel to the CN bond, y-axis in the plane of the ring and z-axis perpendicular to the plane of the ring.) An admixture of some CN double bond character in the planar configuration would only slightly decrease the absolute values for the quadrupole coupling constants in the sp^2-case. From the above values and from the wavefunctions depicted in Fig. 5 we expect the 0^+-state to feature slightly more positive χ_{xx-} ($\hat{=}\,\chi_{aa-}$) and χ_{yy-} ($\hat{=}\,\chi_{bb-}$) values, and a slightly more negative value χ_{zz} ($\hat{=}\,\chi_{cc}$) than the

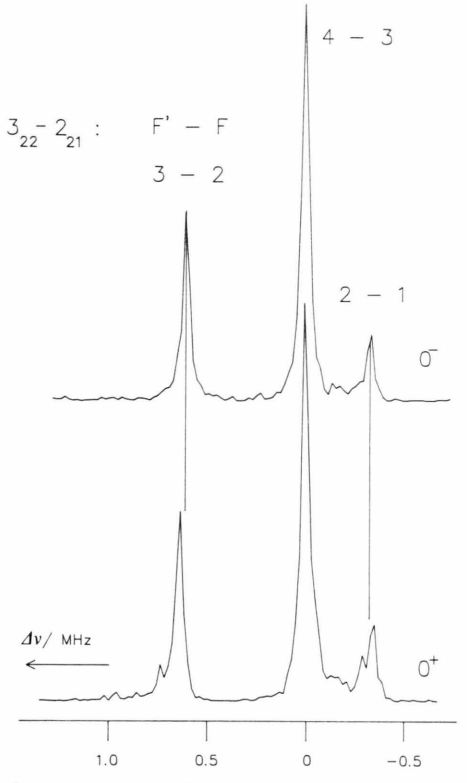

Fig. 5. Upper and lower trace show 2 MHz sections of the ^{14}N quadrupole splitting in the power spectrum of the $3_{22} - 2_{21}$ transition in the 0^--and 0^+-state of the NH_2 inversion mode, respectively (compare Figure 2). The frequencies are given relative to the central $F' - F = 4 - 3$ components. The hfs splittings in the upper multiplet are slightly smaller because of the decrease of the effective (averaged) quadrupole coupling constants when going from the 0^+- to the 0^--state.

0^--state, since in the 0^+-state the planar (and near planar) configurations enter with a higher weight than in the 0^--state, which has a node for the planar configuration.

Just that is observed. We note that similar results are obtained from the nitrogen p-electron densities calculated with the semiempirical CNDO/2 procedure [20], giving $\chi_{xx} = 2.3$ MHz, $\chi_{yy} = 4.0$ MHz and $\chi_{zz} = -6.3$ MHz for an inversion angle $\tau = 37.5°$ and $\chi_{xx} = 3.6$ MHz, $\chi_{yy} = 4.7$ MHz and $\chi_{zz} = -8.3$ MHz for the planar configuration.

However, while these considerations correctly predict the observed trend in the effective coupling constants when going from the 0^+- to the 0^--state, they fail to explain the observed relative magnitude of the χ_{aa}- and χ_{bb}-values. Furthermore the absolute values of the observed coupling constants are considerably

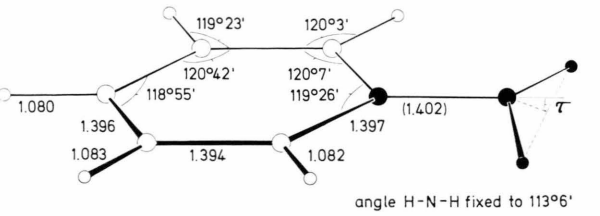

Fig. 6. Perspective view of the aniline molecule showing the parameters and variables used in the semirigid bender calculation described in the text. Except for the CN-bond (see Eq. (1)) and the inversion angle, τ, all structural parameters were kept fixed to their r_s-values [3]. This is also true for the NH-distance (1.001 Å). The bond distances are given in Å-units.

smaller than predicted. Clearly a more sophisticated ab initio calculation is needed for a complete understanding together with an averaging over the inversion motion.

In order to provide the basis for such a quantitative averaging over the correct inversion wavefunctions, we applied the semirigid bender model, developed earlier by one of us successfully for the analysis of the spectra of other molecules undergoing large amplitude internal motions [18].

Our model for aniline is depicted in Figure 6. We assumed a rigid structure for the ring with the bond distances and bond angles frozen to the values of the substitution structure [3]. Also the NH-distance and the HNH bond angle were fixed to their r_s-values. Only the CN bond length was assumed to vary with the inversion angle τ according to

$$r_{CN} = 1.389 + 0.03\,\tau^2, \quad (r_{CN} \text{ in Å}, \tau \text{ in rad}). \qquad (1)$$

In previous studies of cyanamide, formamide and vinylamine [18, 21–23] it had been demonstrated that the inclusion of semirigidity in this bond was of great importance for a correct description of the inversion motion. The shortening of the CN bond length, when going through the planar configuration, simply reflects the build up of some double bond character. Equation (1) was adapted to the aniline case from the results obtained earlier for cyanamide, formamide and vinylamine. For the r_s-value of the inversion angle, $\tau_{r_s} = 37° 29'$, (1) gives the r_s-value for the CN bond length.

With the inversion as the only internal motion in our model, the classical Hamiltonian takes the form (quadrupole coupling still neglected)

$$\mathcal{H} = \tfrac{1}{2}(\mu_{xx} P_x^2 + \mu_{yy} P_y^2 + \mu_{zz} P_z^2 + \mu_{xz}(P_x P_z + P_z P_x)) + \tfrac{1}{2}\mu_{\tau\tau} P_\tau^2 + V(\tau). \qquad (2)$$

In (2) P_x, P_y, P_z are the components of the angular momentum due to the overall rotation. They are referred to the molecular coordinate system. P_τ is the internal momentum, conjugated to the inversion angle τ. Equation (2) is set up in the Eckart-system which for $\tau = 0$ coincides with the principal inertia axes system [24]. Thus there is no kinetic coupling between the overall rotation and the internal momentum P_τ. The elements of the generalized moment of inertia tensor, μ_{xx}, μ_{yy}, etc. are functions of τ and can be calculated from the atom masses and from the structural data presented in Figure 6. For the inversion potential, $V(\tau)$, we assumed a two-parameter quartic/quadratic shape as an approximation with adjustable parameters a and b to fit the experimental data:

$$V(\tau) = a\tau^4 - b\tau^2 + b^2/(4a). \quad (3)$$

For translation into quantum mechanics, (2) was rewritten in Podolsky's form [25]. The corresponding Schrödinger equation for the inversion was solved numerically by the Numerov-Cooley method [26], and the parameters a and b were adjusted for best fit of the far infrared data obtained earlier by Kydd and Krueger [27].

The result is presented in Figs. 3 and 4. The same procedure was also carried out for aniline-ND_2 and for aniline-NHD. For these molecules the same structure was used as for aniline-NH_2 except for the ND bond length, which was assumed to be 0.003 Å shorter than the NH bond to account for the anharmonicity in the stretching vibration. In these calculations the following values were obtained for the central potential barrier, V_b, and for the equilibrium value for the inversion angle, τ_e:

aniline-NH_2: $V_b = 540(5)\,cm^{-1}$; $\tau_e = 44.30(16)°$,

aniline-NHD: $V_b = 575(5)\,cm^{-1}$; $\tau_e = 42.34(15)°$,

aniline-ND_2: $V_b = 556(5)\,cm^{-1}$; $\tau_e = 45.03(21)°$.

We note that the differences of the best values obtained for V_b and τ_e of the three isotopomers most likely reflect differences in the averaging over the other vibrations which of course slightly affects the observed energy differences but which is neglected (except for the NH bond shortening) in our simplified model with only one internal degree of freedom. (For a combined treatment of inversion, torsion and rotation in aniline, the reader is referred to a recent paper by Pyka and Kreglewski [28].)

We further note that cyanamide and vinylamine have barriers very similar to aniline. Also in these three molecules, the effective inversion angle in the 0^+-state is about 6° smaller than the equilibrium angle and about 4° smaller than in the 0^--state.

From the vibrational wavefunctions, numerically determined as described above, we also calculated the vibrational expectation values for τ^2, τ^4 and τ^6. They too are given in Table 3 since they are of use for the comparison of the observed quadrupole coupling constants and theoretical values to be calculated by an appropriate quantum chemical ab initio procedure. Since within the adiabatic approximation the quadrupole coupling constants can be expanded into a Taylor series such as

$$\chi_{gg}(\tau) = \chi_{gg}(0) + \tfrac{1}{2!}\chi''_{gg}(0)\,\tau^2 + \tfrac{1}{4!}\chi''''_{gg}(0)\cdot\tau^4 + \ldots \quad (g = a, b, \text{ or } c)$$

(the uneven derivatives vanish due to the symmetry

$$\chi_{gg}(-\tau) = \chi_{gg}(\tau)),$$

an ab initio calculation of the lowest even- order τ-derivatives of the quadrupole coupling constants together with our vibrational expectation values for τ^{2n} $(n = 1, 2, 3)$ should already reproduce our observed quadrupole coupling constants reasonably well. For cyanamide, NH_2CN, such calculations have been carried out quite recently [21]. They nicely explained the zig-zag-variation in NH_2CN, NHDCN, and in ND_2CN.

Acknowledgements

We would like to thank Prof. H. Dreizler for his help during the build up time of the spectrometer and for critically reading the manuscript. Also the spectrometer could not have been set up without the excellent craftmanship of H. Kähler from the machine shop of our institute. Financial support of Deutsche Forschungsgemeinschaft under grant Su 41/13-1 and from Fonds der Chemischen Industrie is gratefully acknowledged. The numerical calculations necessary to predict and to analyze the spectrum and the CNDO/2 calculations were performed at the PDP10 computer of the University.

Appendix

One-Bit Averaging of Noisy Signals [32]

In a one-bit averager, a plus-one is added to the contents of the "memory" if the input voltage is above

zero, and a minus-one if it is below. In our context "memory" stands for a specific memory cell in a 4k-RAM.

In the following we assume that the input voltage consists of the superposition of a constant signal voltage, U_s, and a noise voltage, U_n:

$$U = U_s + U_n. \tag{A.1}$$

In our special application U_s corresponds to the molecular emission signal at a certain time after the end of the polarizing pulse, and the noise voltage, U_n, can be regarded as truely stochastic since the time interval between probing of equivalent points is at least 12 μs, i.e. long as compared to the noise autocorrelation time in the detection system. For the subsequent quantitative discussion we assume a Gaussian distribution function, $W_n(U_n)$, for the noise voltage. Such a distribution would be generated for instance by a random walk type superposition of the emissions from independent thermal oscillators. It is given by

$$W_n(U_n) = \frac{1}{U_N\sqrt{\pi}}\, e^{-U_n^2/U_N^2}. \tag{A.2}$$

with U_N its $(1/e)$-width (see upper trace in Fig. A1).

The presence of a signal shifts the distribution curve of the input voltage by the amount U_s (see second trace in Fig. A1):

$$W(U) = \frac{1}{U_N\sqrt{\pi^2}}\, e^{-(U-U_s)^2/U_N^2} \tag{A.3}$$

The probabilities, p or m, to encounter a positive or negative input voltage, respectively, are given by

$$p = \int_0^\infty W(U)\,\mathrm{d}U = \frac{1}{2} + \frac{1}{U_N\sqrt{\pi}} \int_0^{U_s} e^{-U^2/U_N^2}\,\mathrm{d}U$$

$$\approx \frac{1}{2} + \frac{U_s}{U_N\sqrt{\pi}}, \tag{A.4}$$

$$m = \int_{-\infty}^0 W(U)\,\mathrm{d}U = \frac{1}{2} - \frac{1}{U_N\sqrt{\pi}} \int_0^{U_s} e^{-U^2/U_N^2}\,\mathrm{d}U$$

$$\approx \frac{1}{2} - \frac{U_s}{U_N\sqrt{\pi}}, \tag{A.5}$$

The linear approximations hold for $U_s \ll U_N$. Now we derive an expression for the distribution function of the averaged memory contents, C, which will be found if the results of a large number of runs, each comprising M repetitive pulse-decay-experiments, are compared.

Let M_+ be the total number of plus-ones and $M_- = M - M_+$ the total number of minus-ones

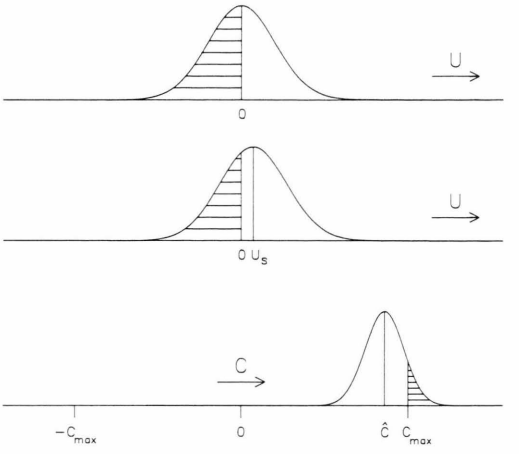

Fig. A1. Voltage distribution functions at the input of the comparator. Upper trace: only noise applied. Center trace: shift by an external signal, U_s. The shaded area represents the probability for a negative input voltage. The lower trace shows the probability distribution for the contents, C, of a storage cell in the RAM, which corresponds to a certain point in the decay of the molecular emission signal. With n-bit words ($n = 16$ in our case), overflow occurs with a probability corresponding to the shaded are at right, if C exceeds $C_{max} = 2^{n-1}$. (For a quantitative discussion see the text.) Note that the scaling is changed when going from the upper two traces to the lower trace. In each case the area under the complete distribution function corresponds to unit probability.

recorded in such an individual run. Then the final contents stored in the memory after accumulation is given by

$$C = M_+ - M_-, \tag{A.6}$$

and the probability for a specific C-value is given by

$$P(C) = p^{M_+} \cdot m^{M_-} \cdot \frac{M!}{M_+!\; M_-!}. \tag{A.7}$$

In (A.7) $p^{M_+} \cdot m^{M_-}$ gives the probability for the occurence of an individual string containing M_+ plus-ones and M_- minus-ones and the binominal coefficient, $(M!/M_+!\,M_-!)$, counts the number of strings with different patterns of plus-ones and minus-ones, but each containing the same total M_+ and M_- numbers.

If we express M_+ and M_- in (A.7) by M and C (see (A.6), and if we approximate the discrete binominal distribution by the corresponding continuous Gaussian distribution [29], we obtain for the distribution function of the C-values

$$W(C) = \frac{1}{\sqrt{8\pi M p m}} \cdot \exp\{-(C - M(p-m))^2/(8 M p m)\}. \tag{A.8}$$

It peaks for

$$\hat{C} = M(p-m) \approx M \frac{2U_s}{\sqrt{\pi}\,U_N} \quad \text{(appr. for } U_s \ll U_N\text{)}. \tag{A.9}$$

and its $(1/e)$-width is given by

$$\Delta C = \sqrt{8\,M\,p\,m}. \tag{A.10}$$

We call C the averaged signal and ΔC the "noise-level" in the averaged signal. As usual, $\hat{C}/\Delta C$ improves proportional to the square root of the number of pulse-decay experiments per run, i.e. to $\sqrt{M}$, and as long as $U_s \ll U_N$, $\hat{C}$ faithfully traces the original signal U_s. We can now relate the ratio U_s/U_N to the likelyhood of a memory overflow, which has to be avoided because it would make the contents of the memory cell useless.

Memory overflow can occur in principle, once M, the number of pulse-decay cycles, has reached the maximum absolute value which can be stored in the memory cell, C_{max}, ($C_{max} = 2^{15}$ for 16-bit registers as used in our case).

For $M > C_{max}$, the outer wing of the C-distribution curve reaches out over C_{max}, and its area (shaded in Fig. A1) gives the probability that an overflow will occur. For instance, if we tolerate an overflow probability of 1/200, the peak of the C-distribution curve at $\hat{C}$ should be positioned about 1.8214 $(1/e)$-widths below C_{max} and we get

$$C_{max} = M_{ovfl} \cdot (p-m) + 1{,}8214 \cdot \sqrt{8\,M_{ovfl}\,p\,m}. \tag{A.11}$$

Equation (A.11) can be solved for M_{ovfl} for each given ratio of U_s/U_N. With $C_{max} = 2^{15} = 32\,768$ and $U_s/U_N = 0.01$ for instance, one finds that it is possible to set the number of hard ware averaging cycles to $M_{ovfl} = 2.54 \cdot 10^6$ with an overflow probability of only 0.5%. (Larger cycle numbers can be realized, if necessary, by secondary software averaging in the computer). In Table A1 we list some combinations of M_{ovfl} and (U_s/U_N)-values for given overflow probabilities, P_{ovfl}.

Table A1. Number of averaging cycles per run in millions, M_{ovfl}, for given signal to noise ratios at the input of the averager, U_s/U_N, and given oberflow probabilities, P_{ovfl}. The values apply for a 16-bit RAM with $C_{max} = 32\,768$. The values given in the column at far right are calculated from the approximation $M_{ovfl} \approx C_{max}/(p-m)$, which leads to reasonable results, once the signal to noise ratio exceeds 0.01. The Table was calculated in analogy to (A.11). The corresponding error integrals were calculated numerically.

U_s/U_N \ P_{ovfl}	1/200	1/100	1/50	1/10	$C_{max}/(p-m)$
0.000 25	50.970	55.000	59.841	76.440	116.2
0.000 50	32.180	34.027	36.183	43.157	58.1
0.000 75	23.854	24.981	26.279	30.374	38.7
0.001	19.071	19.854	20.749	23.531	29.0
0.005	4.807	4.896	4.995	5.286	5.8
0.010	2.540	2.573	2.610	2.716	2.9
0.100	0.279	0.280	0.282	0.285	0.291
0.500	0.062	0.062	0.062	0.062	0.063
1.000	0.039	0.039	0.039	0.039	0.039

We finally turn to the discussion of the dynamic range of the system, i.e. to the question whether the presence of a strong signal will impede the detection of a weak signal.

In the following we will use the symbol U_s for the strong signal and ΔU_s for the weak signal and the question is: "How does the change in $\hat{C}$, which is caused by the weak signal, relate to its value if also a strong signal U_s is present?"

As long as ΔU_s is sufficiently small, this relation can be approximated as

$$\Delta\hat{C} = \left(\frac{d\hat{C}(U_s)}{dU_s}\right) \cdot \Delta U_s. \tag{A.12}$$

With

$$\hat{C} = M(p-m) = M \frac{2}{U_N\sqrt{\pi}} \int_0^{U_s} e^{-U^2/U_N^2}\,dU$$

from (A.9), (A.4), and (A.5), (A.12) immediately takes the form

$$\Delta\hat{C} = \left(\frac{2M}{U_N\sqrt{\pi}}\, e^{-U_s^2/U_N^2}\right) \Delta U_s. \tag{A.13}$$

We call $\Delta\hat{C}/\Delta U_s$ the sensitivity of the system for small signal detection.

As long as the strong signal is still well below the input noise level, i.e. as long as the exponential can be approximated by 1, the presence of U_s has no effect on the sensitivity for detecting ΔU_s. For $U_s = U_N$ however, the small signal sensitivity has already dropped to 36.7% of its peak value, and for $U_s = 2\,U_N$ there is essentially no small signal sensitivity left (1.8% of the peak value).

In our application the strong signal may be of molecular origin due to the presence of a strong molecular transition with a resonance frequency close enough to be polarized by the polarizing pulse. But it may be also due to a coherent pick-up in the electronics of the system or due to a 30 MHz intermediate frequency caused by signal-oscillator microwave leaking to the heterodyne mixer. The later two cases are especially tricky if the spectrometer runs in the "phase alter-

nating pulse sequence mode, since in this mode signals, which do not follow the 180° phase changes, are eliminated before the data are presented to the observer. Thus such a strong perturbing signal can go unnoticed for some time even though it has effectively blindfolded the system.

From the discussion above we can conclude, that one has to change to an ADC with higher resolution, if one is fortunate enough to have better signal to noise ratios at the input, or if coherent pick-ups larger than noise can not be avoided. For a 4-bit ADC for instance with a digitization step height approximately equal to U_N, the small signal sensitivity well be essentially independent on the presence of U_s as long as the latter is still smaller than $7\,U_N$, and for an n-bit ADC and the same digitization step height, the rapid drop in the small signal sensitivity starts when the strong signal exceeds a value of approximately $(2^{n-1}-1)\,U_N$.

[1] D. G. Lister and J. K. Tyler, Chem. Comm., **1966,** 152.
[2] A. Hatta, M. Suzuki, and K. Kozima, Bull. Chem. Soc. Japan **46,** 2321 (1973).
[3] D. G. Lister, J. K. Tyler, J. H. Høg, and N. W. Larsen, J. Mol. Struct. **23,** 253 (1974).
[4] C. C. Costain, J. Chem. Phys. **29,** 864 (1958).
[5] G. Roussy and A. Nonat, Coll. High Res. Mol. Spectr. Riccione, Poster **I,** 26 (1985).
[6] B. Macke and P. Glorieux, Chem. Phys. Lett. **18,** 1 (1973).
[7] J. C. McGurk, T. G. Schmalz, and W. H. Flygare, Adv. Chem. Phys **25,** 1 (1974).
[8] H. Mäder, Methoden und Ergebnisse Mikrowellenspektroskopischer Untersuchungen von Rotationsrelaxation in der Gasphase, Habilitation Thesis, Universität Kiel 1979.
[9] H. Dreizler, Mol. Phys. **59,** 1 (1986).
[10] Ref. 9, Sect. 7.
[11] G. Bestmann, Beiträge zur Mikrowellen Fouriertransform Spektroskopie, PhD Thesis, Universität Kiel 1984, Chapter IV. 6.
[12] U. Andresen and B. Kleibömer, Manuscript submitted to Rev. Sci. Instrum. **1988.**
[13] J. Haekel and H. Mäder, Z. Naturforsch. **43a,** 203 (1988).
[14] W. H. Stolze and D. H. Sutter, Z. Naturforsch. **39a,** 1092 (1984).
[15] H. Barkhuysen, On the Electron Spin Echo Envelope Modulation Technique. Case Studies with Application of Paramagnetic Spectral Analysis PhD Thesis, TU Delft (Netherlands), (1986), Chapts. 1 and 7. Compare too: H. Barkhuijsen, R. de Beer, W. M. M. J. Bovee, and D. van Ormondt, J. Magn. Res. **61,** 465 (1985).
[16] Walter Gordy and Robert L. Cook, Microwave Molecular Spectra, 3rd Edition, John Wiley and Sons, New York 1984, Chapter IX.
[17] Ref. [16]. Appendix C.
[18] Burkhard Kleibömer, Microwave Spectroscopy and Theoretical Models of Nonrigid Molecules, PhD Thesis, Monash University, Melbourne (Australia) 1986.
[19] O. Böttcher and D. H. Sutter, Z. Naturforsch. **43a,** 47 (1988).
[20] J. A. Pople and D. L. Beveridge, Approximate Molecular Orbital Theory, McGraw-Hill Book Company, New York 1970. The original parametrization was used in our calculations.
[21] R. D. Brown, P. D. Godfrey, M. Head-Gordon, K. Wiedemann, and B. Kleibömer, J. Mol. Spectros. in print (1988).
[22] R. D. Brown, P. D. Godfrey, and B. Kleibömer, J. Mol. Spectros. **124,** 34 (1987).
[23] R. D. Brown, P. D. Godfrey, and B. Kleibömer, J. Mol. Spectros. **124,** 21 (1987).
[24] V. Szalay, J. Mol. Spectros. **102,** 13 (1983), and references cited therein.
[25] E. C. Kemble, The Fundamental Principles of Quantum Mechanics. Dover Publ., New York 1958, Chapt. XI, Sect. 48c.
[26] J. W. Cooley, Math. Comp. **15,** 363 (1974).
[27] R. A. Kydd and P. J. Krueger, Chem. Phys. Lett. **49,** 539 (1977).
[28] J. Pyka and M. Kreglewski, J. Mol. Spectrosc. **109,** 207 (1985).
[29] F. Reif, Statistical Physics. Berkeley Physics Course, Vol. **5,** McGraw-Hill Book Company, New York 1964, Appendix A.1.
[30] W. Hüttner and W. Majer, Mol. Phys. **52,** 631 (1984).
[31] D. Papoušek, J. M. R. Stone, and V. Špirko, J. Mol. Spectrosc. **48,** 17 (1973).
[32] For a discussion of the effects of one-bit averaging and of the shape of the noise distribution function on the determination of relaxation times and -phases from transient decays see J. Haekel, Diplom thesis, Universität Kiel 1985.